

Exploring Halide Melting Behavior with CHGNet and Advanced Simulation Techniques

Joachim Scheerlinck¹, Sunny Gupta², Bowen Deng³, and Gerbrand Ceder⁴

^{1,2,3,4}*Materials Sciences Division, Lawrence Berkeley National Laboratory, California 94720, United States*

^{2, 3, 4}*Department of Materials Science and Engineering, University of California, Berkeley, California 94720, United States*

(Dated: October 12, 2023)

In the last 70 years, there have been significant improvements in both computer hardware and computational efforts such as machine learning (ML). From self-driving vehicles to identifying exoplanets, ML has proven its value in our modern day world. With an increasing need for energy storage comes a rising demand to find the right materials to create more energy dense and durable batteries. One of the ways ML is involved in tackling this problem, is through machine learned interatomic potentials (MLIPs). Recently, CHGNet (or the Crystal Hamiltonian Graph Neural Network) was developed by B. Deng et al., 2023. CHGNet is trained on density functional theory (DFT) calculations from the Materials Project Database that span the whole periodic table. Different from previous MLIPs, CHGNet has built-in charge information. Thanks to the extensive database's accessibility and the inclusion of built-in charge information, CHGNet attains state-of-the-art performance in managing large-scale atomistic simulations characterized by intricate electron interactions. In this study, we tested CHGNet's ability to determine melting points, particularly in the halide materials that draw growing attention in all-solid-state-batteries. We compared the melting point predictions from multiple methods including the Hong model, the heating curve method (continuous heating), the two phase coexistence method and some cohesive energy calculations. By critically benchmarking across the different methods, we show that universal interatomic potentials are not always accurate in dynamic simulations. With analysing on the failure modes, we propose possible reasons and improvements that can be made for future universal interatomic potentials.

I. Introduction

The melting point of a compound is a fundamental property that derives from the interactions at atomic scales. The importance of melting points drives the application in heat shields, hypersonic vehicles and biochemical, pharmaceutical, and environmental sciences (Jain & Yalkowsky, 2006). Calculating melting points as a way to characterize materials provides insights into the structural changes, stability and energy requirements associated with the transition from the solid phase to the liquid phase. Furthermore, these insights help optimize industrial process parameters, e.g. production efficiency and material selection (Khare et al., 2012; Ljungberg, 2007; Ge et al., 2013). Overall, determining melting points plays a vital role in advancing in numerous scientific disciplines.

Traditional materials discovery approaches, implemented to enhance material selection, typically have long timeframes (up to 20 years on average). (Z. Deng et al., 2022; Cole, 2020). The synthesis and characterization of each individual material may take months to years (Mroz et al., 2022). In addition, many newly discovered materials, such as new species of minerals, are accessible in limited amounts (Hong et al., 2022). This makes measuring melting points experimentally quite challenging. As the capabilities of computers continue to improve exponentially and experimental limitations are not present, computational efforts

have become increasingly useful for the general and accurate modeling of materials (Cyganiak et al., 2009; Thompson et al., 2022). Although these experimental limitations are not present, other difficulties arise: The requirement of large simulation cells, long simulation trajectories, and the dependence on auxiliary empirical potentials challenge DFT-based melting point computations (Hong, 2015). Furthermore, it is important to note that computational predictions are not always accurate, and they should be validated experimentally whenever possible. Therefore, the ideal material discovery approach has the accuracy of real life experiments and the efficiency of computational efforts.

Computational techniques still offer a promising path for characterizing materials and understanding their structural changes during phase transitions. Development in modeling methodologies like large-scale atomistic simulations show capability of accelerating material design. For example, design of new catalysts: Catalysts are used to speed up chemical reactions, and are essential for many industrial processes. Large-scale atomistic simulations can be used to design new catalysts with higher activity and selectivity (Jinnouchi et al., 2020). Development of new batteries: Batteries are used to store energy, and they are essential for many emerging technologies, such as electric vehicles and renewable energy storage. Large-scale atomistic simulations can be used to develop new battery

materials with higher energy density and longer cycle life (Bianchini et al., 2022). Design of new materials for solar cells: Solar cells are used to convert sunlight into electricity, and they are a key technology for renewable energy. Large-scale atomistic simulations can be used to design new solar cell materials with higher efficiency and lower cost (Hutter et al., 2014).

While the high melting points of most inorganic ionic compounds pose challenges for experimental measurement, the rapid advancement of computational techniques, despite their own complexities, offers a promising avenue for accurately characterizing materials and understanding their phase transitions. Large-scale atomistic simulations hold great potential for diverse applications, from designing more efficient catalysts to developing advanced battery materials and cost-effective solar cell materials, thus contributing significantly to the advancement of various industries and emerging technologies.

On a different note, the cars we drive evolve, and our expectations of these newer models evolve with them. One of the main concerns for the electric car of the future is safety. This is why in the last decade battery safety has been such a hot topic in the research community, especially given how difficult it is to extinguish a battery fire (Victor Chombo et al., 2021). While lithium-ion batteries (LIB's) have revolutionized energy storage, safety hazards originating from the flammability of these liquid electrolytes pose significant threats to the further advancement of LIB technologies (Kwak et al., 2022). Regarding these threats, all-solid-state-batteries have recently gained increasing interest with intrinsic safety and high energy density in mind (Kato et al., 2016; Abakumov et al., 2020; Li et al., 2020; Yang et al., 2021). In particular halide solid state electrolytes (SSEs) have proven to be promising. For instance Li_3YBr_6 (Asano et al., 2018) and Li_3InCl_6 (Li et al., 2019) SSEs can be synthesized by liquid phase methods, show good compatibility with oxide cathodes, and display high ionic conductivities around $10^{-3} \text{ S cm}^{-1}$ (Hu et al., 2018; Li et al., 2019). From this, we conclude that the research focus on halide conductors presents a reasoned pathway to enhance battery safety and advanced all-solid-state-battery technology in general.

A. CHGNet

In general, a relatively computationally inexpensive way of performing molecular dynamics is by using empirical potentials. However, these depend on the reliability and availability of such empirical potentials (Jorgensen & Tirado-Rives, 1988). Even more so, accurately building new classical potentials for every new material would be extremely time consuming. Density Functional Theory (DFT), which calculates energy and forces from ab initio, provides greater generality and reliability. Nevertheless, DFT methods remain notably expensive (Simón & Goodman, 2011). This is where machine-learned interatomic potentials (MLIPs) come in to the picture. By learning from the

comprehensive atomic structures generated from DFT, MLIPs provide the chance for high precision simulation without having to do DFT calculations for every material, which enables the opportunity for faster and larger simulations. Furthermore, as written in B. Deng et al., 2023, MLIPs such as ænet (Artrith et al., 2011; López-Zorrilla et al., 2023) and DeepMD (L. Zhang et al., 2021) are both promising efforts to combine the quantum-mechanical accuracy of explicitly computing (very costly) electronic structures with the efficiency of classical interatomic potentials. Specifically, graph neural network (GNN)-based MLIPs such as DimeNet (Gasteiger et al., 2020), NequIP (Batzner et al., 2022), and TeaNet (Takamoto, Izumi, & Li, 2022) have been shown to achieve state-of-the-art performance. GNN-based MLIPs trained on the periodic table, M3GNet (C. Chen & Ong, 2022), for example, have demonstrated the possibility of universal interatomic potentials that may not require chemistry-specific training for each new application (Choudhary et al., 2023; Takamoto, Shinagawa, et al., 2022).

Recent development allows the description of charge in MLIPs B. Deng et al., 2023. The inclusion of the important effects of valences on chemical bonding remains a challenge for MLIPs (Unke et al., 2021; Ko et al., 2021; Zubatyuk et al., 2021). While traditional MLIPs treat the elemental label as the basic chemical identity, different valence states of transition-metal ions behave as different from each other as different elements. Even more so, the Jahn-Teller effect can cause strong chemical interaction variability across different valence states. This variability exists for almost all transition-metal ions and requires the specification of an ion beyond its chemical identity. In addition, the charge state is a degree of freedom that can create configurational entropy and whose dynamic optimization can lead to strongly coupled charge and ion motion, which is impossible to capture with an MLIP that carries only elemental labels. The relevance of explicit electron physics motivates the development of a robust MLIP model with built-in charge information. CHGNet does just this.

CHGNet or the Crystal Hamiltonian Graph Neural Network is a pretrained universal neural network potential for charge-informed atomistic modelling (B. Deng et al., 2023). The foundation of CHGNet is a GNN, a type of machine learning algorithm that is used to model data represented as a graph. In the context of CHGNet, the graph represents the crystal structure of a material, which makes CHGNet a structure-based model. It is trained on a dataset of DFT calculations. More specifically, CHGNet is pretrained on the energies, forces, stresses, and magnetic moments from the Materials Project Trajectory dataset, which consists of over 10 years of density functional theory calculations of more than 1.5 million inorganic structures (Jain et al., 2013). To accurately sample the universal potential energy surface (PES), Deng et al. extracted 1.37 million structure relaxation and static calculations tasks from the Materials Project Database that spans the whole periodic table. This resulted in

a comprehensive Materials Project Trajectory (MPtrj) dataset with 1,580,395 atom configurations, 1,580,395 energies, 7,944,833 magmoms, 49,295,660 forces and 14,223,555 stresses. Due to the accessibility of such an enormous database and the built-in charge information, CHGNet achieves state-of-the-art performance for large-scale atomistic simulations with complex electron interactions (Riebesell et al., 2023). With these early benchmarks that shows their capability, MLIPs like CHGNet emerge as promising new tools for atomistic modeling, that are expected to have a significant impact on materials science in the coming years.

B. Existing melting point methods

Over the last few decades many methods have been developed to predict melting points computationally. Most of them use a box full of atoms, where the atomic movements are simulated using techniques such as molecular dynamics (MD) and Monte Carlo (MC). The melting point is then determined by studying the evolution of the liquid and fluid involved in the phase transition.

1. Heating methods

One of the least complex procedures involves performing several constant pressure and temperature simulations on a solid material (a perfect lattice), with each simulation having the same pressure, but a different temperature. From the resulting trajectories, the density can then be determined. Subsequently, the temperature at which the density shows a discontinuity, at which the lattice breaks down, is taken as the melting point. This method is called the heat-until-melts method from M. Chen et al., 2013. Some parts of the accuracy of this method, however, will be determined by the number of NPT simulations, which, with an increasing number, become increasingly costly. Despite this, searching for a discontinuity remains, in theory, a good idea. Therefore a secondary heating method incorporating this fundamental concept, but circumventing this limitation, will be used in this study.

A not aforementioned issue of the Heat-until-melts method is the following: The procedure only provides an upper bound to the melting point because it overestimates the transition temperature due to superheating effects (Chokappa & Clancy, 1987). For instance, the predicted melting point of Lennard-Jones particles is 14 percent too high at zero pressure (Chokappa & Clancy, 1987). Note that the existence of superheating, this hysteresis phenomenon is also true in the reverse process: Cooling a liquid down results in supercooling, underestimating the transition temperature (Agrawal et al., 2003). Using both supercooling and superheating effects, the hysteresis method was developed (Luo et al., 2003). Finding the overestimated transition temperature is usually not the problem, but finding the underestimated transition temperature is. This is the case because crystal nucleation is a rare event. Although the glass transition temperature can roughly

be taken as the supercooled transition temperature, the hysteresis method has relatively low accuracy (Zheng et al., 2006). From this, we conclude that it is wise to look into different methods as well.

2. Voids method

Experimentally, hysteresis is not a problem even slightly superheating solids is usually quite difficult. This is due to heterogeneous nucleation: defects act as nucleation sites for the liquid phase as the crystal is heated. These defects may be vacancies, dislocations, or surfaces; in fact, some surfaces become disordered well below the bulk melting temperature (Morris et al., 1994). Unlike the heat-until-melts method, the voids method exploits this, but, similar to it, it also uses (density) discontinuities. In this method, voids or defects are created in a perfect crystal lattice, to lower the nucleation free energy barrier, making it possible to observe melting on the MD simulation (finite) length and timescales. More over, after equilibrating the solid structure closest to the void will collapse and local pockets of liquid structure form. This effectively leads to multiple solid-liquid interfaces, which lower the free energy barrier for the solid to liquid transition. This method can also be summarized by performing multiple heat-until-melts procedures and varying the number of voids. With increasing void density, the melting point converges and becomes independent of the number of voids Alavi & Thompson, 2006). It should be noted, however, that the final number of voids needed for this convergence is not initially known and may vary between materials. Even more so introducing too many voids often leads to unstable simulations, where a collapse of the solid is observed without a discontinuous phase change (Phillpot et al., 1989). Knowing this, the voids method is not examined in this study.

3. Free energy methods

Be that as it may, this sparks interest in different methods to predict the melting point of a material. In particular can this be done by analyzing thermodynamic properties such as the free energies of the system (Hong, 2015). At the melting point T_m , the crystal and liquid phases of a substance can coexist in equilibrium, at which the Gibbs free energy of the two phases becomes the same. The crystal phase has lower free energy at temperatures below T_m and is therefore the more stable phase. Melting occurs when the temperature exceeds T_m and the free energy of the crystal becomes higher than that of the liquid phase. In other words, the system can spontaneously adjust its temperature. The equality of the free energies (stability) of both phases then determines the melting point (Mei & Davenport, 1992). Numerous methods to calculate the free energy are available such as the umbrella sampling method (Kästner, 2011), the thermodynamic integration method (Mitchell & McCammon, 1991) and the free energy perturbation method (Singh & Kofke, 2004). Although appealing, free energy calculations are in general computationally expensive (Perez et al., 2016) and is therefore not

investigated further in this study.

4. Two phase coexistence method

In retrospect, looking back at the voids method, the small local solid-liquid interfaces in the voids method embolden the idea of inducing solid-liquid interfaces without necessarily using voids. Taking this into consideration, having a two phase coexistence remains an intriguing approach. Although many variants on the two phase coexistence method exist (Y. Zhang & Maginn, 2012; Larsson Sihm, 2019), this study will largely use the two phase coexistence model of Alavi & Thompson, 2006 as a basis. In this review paper, the following method is discussed: In simulations of coexisting solid and liquid phases in contact (such as in Morris et al., 1994) the system already has the necessary free energy for the formation of a solid-liquid interface. Equal amounts of solid and liquid are equilibrated separately to a desired temperature, respectively, below and above the melting point. The solid and the fluid structures are then merged along the x direction, creating a 2 phase simulation cell, with equal cross sections in the yz direction.

In figure 1, an example is given of a monoatomic model system’s initial configuration for a two-phase coexistence simulation. In the middle of the simulation cell, there is a contact surface between the solid and the liquid. At the edges of the simulation cell, due to periodic boundary conditions (in the x-direction), there will be a second contact surface in the yz-plane. The two-phase cell is then relaxed with an NVT simulation to allow the molecules, primarily at the contact surface, to relax to more stable positions. Followed by a NVE simulation, part of the solid will melt or part of the liquid will crystallize, causing a redistribution of the potential energy and kinetic energy, causing the simulation temperature to change. This process continues until the temperature converges at a certain simulation pressure, resulting in solid-liquid equilibrium. This method requires long simulation times and large simulation cells to obtain converged melting point values. At least 880 atoms are required to minimize surface effects on the thermodynamics of melting (Agrawal et al., 2003; Solca et al., 1997). It should also be noted that two phase coexistence simulations using an NPT simulation instead of an NVE simulation are also common. However, it was found that the crystal-liquid interface is more often maintained using an NVE simulation rather than an NPT simulation (Y. Zhang & Maginn, 2012). Therefore in this study, the NVE approach is used.

5. The ML model from Qi-Jun Hong et al

Well aware of the shortcomings of the above and other methods, Qi-Jun Hong and coworkers published a paper on melting temperature prediction using machine learning (ML) (Hong et al., 2022). A ML model was built to predict the melting temperature, with the ultimate goal of integrating DFT and ML,

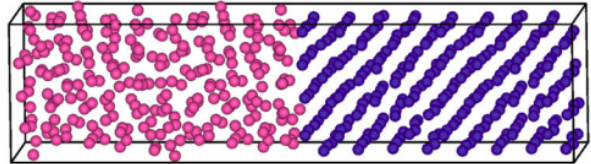


Figure 1: Geometries for the coexistence structure of solid (blue) and liquid (pink) phases at 434 K of the initial geometry of Li (M. Chen et al., 2013)

which complement each other in terms of speed and accuracy. The ML model allows rapid estimation of melting temperatures, at a speed on the order of milliseconds per material, while the DFT calculation provides robustness and accuracy at a much higher cost on the order of several days of computations per material. The database used to train and test the model consists of chemical compositions (i.e., elements and concentrations) or equivalent chemical formulas of the materials and their corresponding melting temperatures.

The database consists of DFT melting temperature calculations from Hong & Van De Walle, 2016, together with melting point data from Glushko & Gurvich, 1988, with the latter also being the basis for this study. The machine learning model combines the Graph Neural Network (GNN) (Scarselli et al., 2008) and residual neural network (ResNet) (He et al., 2016) architectures within the Tensorflow (Abadi et al., 2016) framework. When a material (i.e., its elements and composition) is fed to the neural network, each element is first converted to 14 features, such as atomic radius, atomic mass, electronegativity, core and valence electrons, ionization energy, electron affinity, density, and position in the periodic table. The training process required 2,000–4,000 epochs of optimization. The melting temperature database contains 9,375 materials, of which 8,635 and 740 materials were randomly assigned to the training set and testing set, respectively. Furthermore, the root-mean-square errors (rmse) of the predicted versus actual melting temperature (as can be seen in figure 2) were reported to be 110 and 160 K for the training and testing sets, respectively. Note that these surprisingly small errors (DFT error is typically 100 K (Hong, 2015) due to imperfect density functionals) represent the method’s accuracy over the ranges of composition that are included in the database. Furthermore, the score of the model (R^2 : 0.933, rmse: 160K) outperforms that of XGBoost (R^2 : 0.919, rmse: 183K) (Hong et al., 2022). From this and the universality of the model we conclude that the Hong model is a good fit for use as a benchmark in our melting point prediction study.

C. Visualization methods

In this study, while using some of the aforementioned methods, we are particularly interested in phase change information about the system. More specifically, we are interested in determining whether the system fully

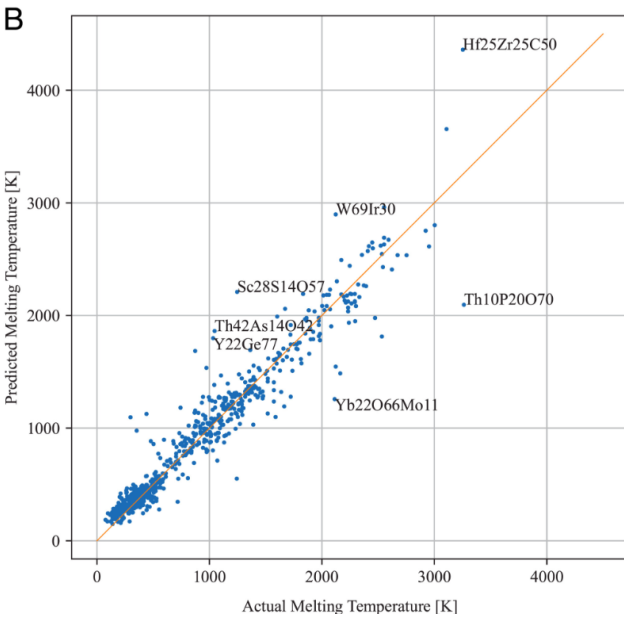


Figure 2: Predicted vs. actual melting temperatures in the testing dataset. Compounds with large errors are labeled (Hong et al., 2022).

liquefies, solidifies, or remains partially liquid and partially solid with a moving interface. The following methods of visualization pose as an aid in doing just this.

1. Radial Distribution Function

The Radial Distribution Function (RDF), also known as the pair distribution function or pair correlation function, describes the radial frequency and intensity of surrounding matter with respect to a reference point. It is a statistical measure of the likelihood of finding another particle at a given distance from a reference particle. In an infinite crystal lattice, ions of the same type occur and reoccur regularly at set distances from any arbitrary starting point. As this is not the case for a liquid, the RDF of a liquid is different to that of a structured solid, such as a periodic crystal. The absence of any periodicity in the RDF indicates that the structure is a fluid or an amorphous solid (Larsson Sihm, 2019). Even more so, because the NVE always starts with a 50 % solid structure, this always indicates the occurrence of melting, regardless of whether it remains a liquid or solidifies immediately after. An example of how to interpret RDFs is given in figure 3. At 300 K, the system is solid in a crystal structure. With Na^+ as a reference, the first peak stems from the ionic bonds with the six chloride ions closest by. Similar subsequent peaks in the RDF indicate the periodicity of the crystal structure. The absence of any crystalline structure at higher temperatures in Figure 3 is clearly identified by the amplitudes rapidly declining and the curves flattening at larger distances (Larsson Sihm, 2019). As the difficulty in using this method lies in distinguishing an amorphous crystal from a liquid, different methods are also needed.

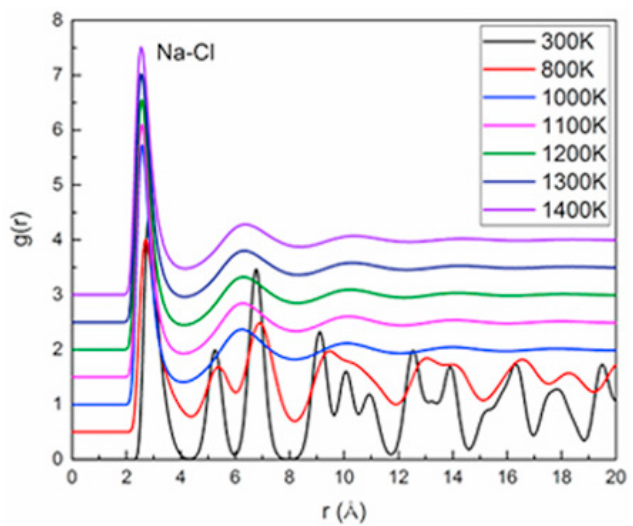


Figure 3: RDF for Na-Cl interaction in a simulated eutectic NaCl-KCl (50-50 mol%) salt at different temperatures (Ding et al., 2017). The salt is molten at all temperatures, except 300 K

2. Visualisation of the structure

The system's structure can be visually inspected with any molecular visualization software, such as Ovito or Vesta, by using a CIF file as input. Rather easily, it can be determined whether the system has (periodic) structure, found in crystals, or is unorganized, characterizing either a molten or an amorphous system. While this may be tedious, it has the advantage of showing local structural information that cannot be identified with other methods, e.g., if the system has completely solidified/liquefied or not (Larsson Sihm, 2019).

3. Evolution video

From trajectory files it is possible to create hundreds of CIF files at different points in time. From these files, using Ovito, a video showing the time evolution of the system can be created. Using this video, it becomes rather easy to determine whether a system is fully liquid or solid (Larsson Sihm, 2019). However, as the ability of human eyes is limited in detecting fine details such as small movements, this makes this method prone to human error. Fortunately, in Ovito it is possible to add another layer to the visualization, a layer of mean square displacement. To show this mean square displacement, a reference frame is required. Note that taking only the first frame, the initial system as the reference frame, can result in missing solidification after 150 ps. Therefore, it is necessary to visualize the results with a later reference frame as well. Hence, giving every atom a color based on its mean square displacement successfully creates an extra way to visualize phase changes within the structure.

II. Results

The following models were tested during this study: the Hong model, the heating curve method (a revised

heat until-melts-method) and the two phase coexistence method. Note that, accept for the Hong model, during every first test we investigated aluminum. This is because testing the models with a well-known aluminum potential, before using CHGNet, provides us with essential information about these methods.

A. The Hong Model

The first step in predicting melting points for halides is determining whether there is room for improvement. From Figure 2, we can determine that there is room for improvement based on the labeled outliers. These outliers, however, are not halides. Therefore, it is necessary to test the Hong model, focusing on halides. We extracted the experimental melting point data of 56 halides from Glushko & Gurvich, 1988, using the “TKV Database”, n.d. After testing the Hong model on these 56 halides and comparing the results with the experimental data, it was possible to make a similar plot for the halides (see Figure 4).

First, the rmse for the halides is 215 K, which is more than the 160 K that was provided in the paper. To put this into perspective, this means that the difference from the RMSE of typical DFT calculations (100 K) has nearly doubled. Note that there are also errors on the experimental data, but these are simply too small to be noticeable. Second, the Pearson correlation coefficient of the 56 halides is 0.89, which is slightly worse than that of the 2022 Hong paper ($R^2: 0.93$), but it is still quite good. Taking a look at the outliers, we find HfF_4 , TiI_4 and TiBr . One explanation could be that, as mentioned by Hong et al., 2022, accuracy can degrade for predictions requested in relatively poorly sampled regions of composition space, as this demands considerable extrapolation. It is possible that HfF_4 , TiI_4 , TiBr lie in poorly sampled composition space. However, these may also be outliers because of their structure or high temperature. They resp. Have a 3D, 1D, and 2D structure. The fact that this model is a composition-based model might explain why it has more difficulty accurately predicting the melting points of certain structures. Combining everything, the increased rmse, the smaller Pearson correlation coefficient and the outliers, are clear signs that there is still room for improvement. Therefore, we can conclude that predicting halide melting points with a structure-based model such as CHGNet will be particularly interesting.

B. Heating Curve Method

As mentioned before, the heat-until-melts method, with discrete points, is certainly not ideal. Therefore, a new, but fundamentally similar, idea was used. Instead of a small number of discrete points, nearly continuous adiabatic heating was used. After every small timestep, a relatively fast NPT simulation is performed. In this revised method, heating sufficiently slowly should ensure adiabatic heating.

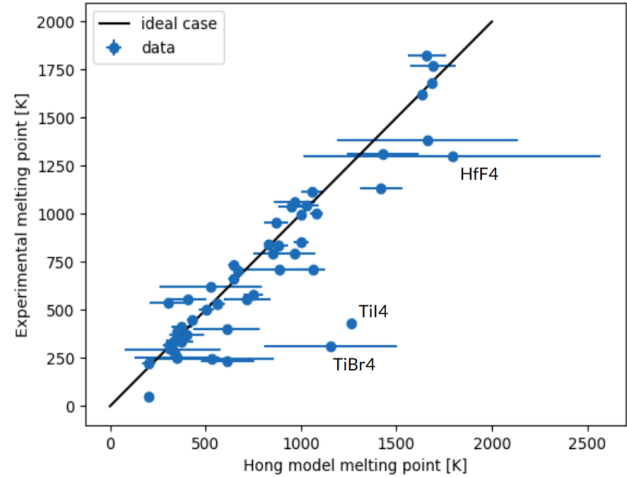


Figure 4: Actual vs. predicted melting temperatures of 56 halides. Compounds with large errors are labeled. The ideal case, where the prediction matches experiment, is shown as a black line.

1. Aluminum: LAMMPS

The following procedure for aluminum, using LAMMPS (Plimpton, 1995), was followed: Using the classical potential from Mendelev et al., 2008, we created a supercell from the Al FCC unitcell. Second, to thermalize the system, a 20 ps NVT simulation at a temperature of 100 K is performed. Third, the system is subjected to a 1 ns NPT simulation from 100 K to 2000 K. During the NPT simulation, the enthalpy and the temperature is outputted. Similar to the heat-until-melts method, we identify the melting point with the discontinuity in the enthalpy. This was done for a 4x4x4, a 7x7x7 and a 10x10x10 supercell, with, respectively, 256, 1372 and 4000 atoms. The results are visualized in Figure 5. This normalized enthalpy vs. temperature plot shows that the 4x4x4 supercell has too much noise. As expected, the noise decreases with the number of atoms. With 1372 atoms, the 7x7x7 has a similar amount of noise as the 10x10x10 supercell containing 4000 atoms. This is why for future use, care should be taken to use a sufficient amount of atoms. To verify the observed discontinuities, the temperature is also plotted with respect to time in Figure 6. From this, we can again confirm that the structure has melted. Furthermore, with linear regression, we find that the system was heated at a speed of 1.91 K/s. Note that 4x4x4 supercell shows a speed of 1.9 K/s and not 1.91 K/s due to noise.

For the exact calculation of the melting point, the derivative of the enthalpy is calculated. As mentioned above, we only need the 7x7x7 data, and will disregard the 4x4x4 supercell simulation. Just for comparison, the 10x10x10 will also be processed further. Given that the derivative of a quantity with noise only gives even more noise, a few data manipulations are performed. For starters, is the enthalpy averaged out for every 10 K, which is shown in yellow in Figure 7. In the ideal case, we would see a jump in enthalpy and two linear regions. Unfortunately, however, the data still have too much noise. Second, a Savitzky-Gollay

filter, a method of data smoothing based on local least-squares polynomial approximation (Schafer, 2011), is used twice on the enthalpy, before taking the derivative. These filtered data are shown in blue in Figure 7.

From this filtered data, we can identify three regions, a low-temperature regime with a quasi-constant enthalpy derivative, a mid-temperature regime with two peaks in the enthalpy derivative, and a high-temperature regime with a quasi constant enthalpy derivative. From thermodynamics, we expect only one peak. Similar to the heat-until-melts method, there appears to be a superheated solid. The fact that there are two peaks signifies that the superheated solid, melts a bit, stops melting, becomes superheated again, and then fully melts. From the high- and low-temperature regimes the average enthalpy gradient and standard deviation are calculated. From the three sigma rule, it is known that 99.7% of the data is contained within three times the standard deviation around the average. The remaining 0.3% of the data that's outside of this regime, can be called outliers. Knowing all this, determining the melting point and it's error boils down to determining the first low-temperature outlier in middle regime and the last high-temperature outlier in the middle regime.

Having a superheated solid makes it difficult to precisely pinpoint the moment of melting; therefore, the melting point is taken as the temperature in the middle of the error-range. From this procedure, the results are $1040 \text{ K} \pm 160 \text{ K}$ for the $10 \times 10 \times 10$ supercell and $1020 \text{ K} \pm 190 \text{ K}$ for the $7 \times 7 \times 7$ supercell, as shown in Figure 8. Comparing this to the experimental melting point of aluminum, which is 933 K (Glushko & Gurvich, 1988), the $7 \times 7 \times 7$ supercell predicted melting point is only 11 % larger than the observed melting point. Compared with the 14 % of Chokappa & Clancy, 1987, this is a slight improvement. The error on this melting point (190 K) however, is still quite large compared to the 160 K from the Hong model (Hong et al., 2022). As expected, the $10 \times 10 \times 10$ supercell predicted melting point has a smaller error. Note that the error on the predicted melting point of this method might depend on the filtering. Nevertheless, given the results in Figure 7, we can assume these effects to be minimal. In conclusion, the heating curve method is suboptimal, but sufficiently accurate to study the ability of CHGNet to determine melting points.

2. Aluminum: CHGNet

After testing the empirical aluminum potential with LAMMPS, the CHGNet predicted aluminum potential was tested with ASE (Larsen et al., 2017a). We again used a $7 \times 7 \times 7$ Al supercell. Some modifications were made. To thermalize the system to a temperature of 400 K , a 10 ps NPT simulation was performed, after which a 10 ps NPT equilibration was performed at 400 K . Finally, a second NPT simulation was performed

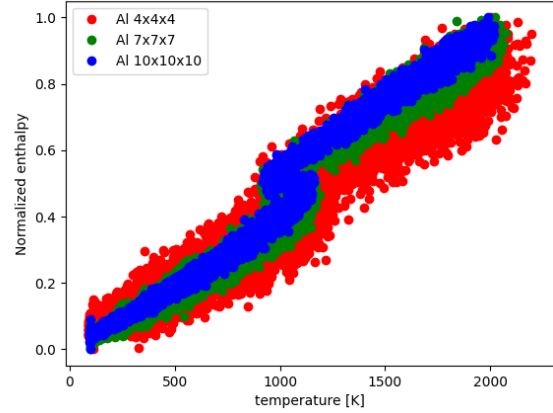


Figure 5: Enthalpy with respect to temperature of the heating curve simulations in LAMMPS of Al for a $4 \times 4 \times 4$, a $7 \times 7 \times 7$ and a $10 \times 10 \times 10$ supercell.

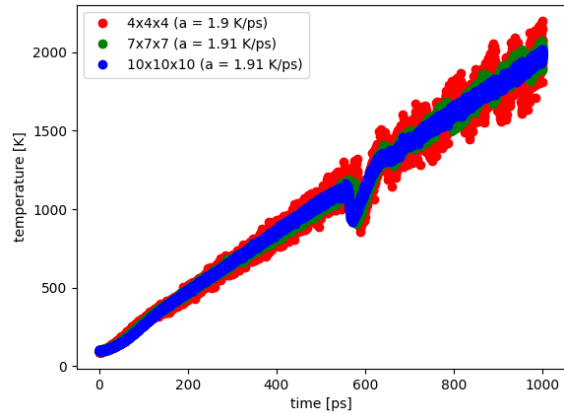


Figure 6: Temperature with respect to time of the heating curve simulations in LAMMPS of Al for a $4 \times 4 \times 4$, a $7 \times 7 \times 7$ and a $10 \times 10 \times 10$ supercell.

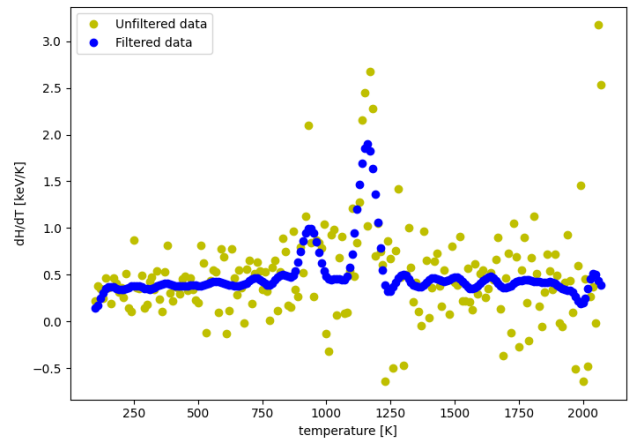


Figure 7: Filtered and unfiltered enthalpy gradient with respect to temperature of the heating curve simulations in LAMMPS of Al for a $7 \times 7 \times 7$ supercell.

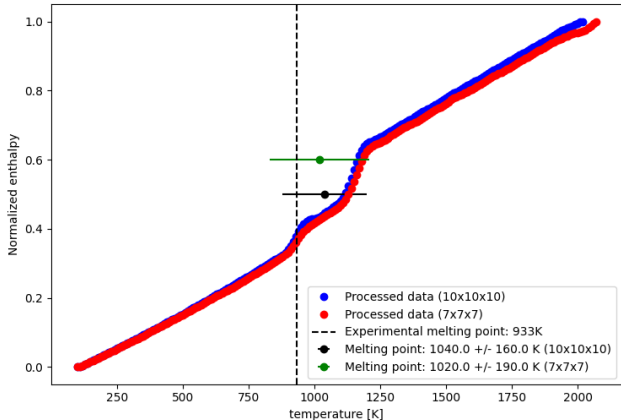


Figure 8: Processed (averaged out every 10K and filter) normalized enthalpy with respect to temperature of the heating curve simulations in LAMMPS of Al for a 7x7x7 and a 10x10x10 supercell.

to heat the temperature to 1200 K. During the NPT simulations, a temperature coupling constant (taut) of 50 fs was used. Following the same data processing procedure as before, the results for aluminum from the second NPT simulation are given in Figure 9. The final result is a CHGNet predicted melting point of 795 K with an error of 105 K. The error is now comparable to the error from DFT (Hong, 2015), which we can intuitively expect from a machine-learned model based on DFT calculations. Although the error is much smaller compared to the error for the empirical potential in LAMMPS (160 K), the experimental melting point is no longer within the range of error. From this we can clearly observe that CHGNet underestimates the forces, resulting in a lower predicted melting point for aluminum.

C. Halides: CHGNet

From aluminum, we move on to halides, which are the focus of this study. The first halides tested are the outliers from the Hong model (for halides): HfF₄, TiI₄, TiBr₄ and two reference halides: WCl₆ and LiCl. Note that for these halides, the supercell will never have more than 500 atoms to ensure computational efficiency.

1. LiCl

For LiCl, the heating curve method was followed with a supercell containing 432 atoms, a starting temperature of 300 K (instead of 400 K), and an end temperature of 1100 K. The reasoning behind this temperature range as for the temperature range of the other halide simulations is to simulate a close but broad enough range around where we expect the melting point to be. For LiCl for instance, the experimental melting point is 833K (Glushko & Gurvich, 1988). As we noticed from the aluminum simulation that CHGNet seems to predict a lower melting point, it makes sense to use a 400 K range around 700K. The results of the second NPT simulation using LiCl are visualised in Figure 10. CHGNet predicts a melting point of 660K with an error of 100K. Similar to the case of aluminum, CHGNet

again produces an error similar to errors based on DFT calculations. Furthermore, CHGNet consistently underestimates the interatomic forces, leading to its prediction of a lower melting point of 660K \pm 100K, with the experimental melting point of 833K falling outside the error range.

2. HfF₄

For HfF₄, a supercell containing 480 atoms, a starting temperature of 300 K, and an end temperature of 2000 K was used. The results are visualized on a temperature-time plot in Figure 11 in yellow. From this, we notice something peculiar: although the system has not melted yet, which was confirmed with OVITO (Stukowski, 2009), the temperature stagnates in the proximity of a temperature of 800 K. This result might be related to the high experimental melting point of HfF₄, which is 1298 K \pm 20 K (Glushko & Gurvich, 1988). Due to the limited time of this study, this was not further looked into, as quantifying the effectiveness of CHGNet in general has a higher priority.

3. TiBr₄

For TiBr₄, a supercell containing 480 atoms, a starting temperature of 100 K, and an end temperature of 1000 K was used. The result of the second NPT simulation is again visualized on a temperature-time plot in Figure 11 in red. The simulation was aborted before 1 ns because it had already melted, which was confirmed with OVITO (Stukowski, 2009). Taking a look into the first NPT simulation, meant to equilibrate the system at 100 K, we find some answers. The density-time plot in Figure 12 shows three very distinct regions. In 10 ps, the system goes from solid to liquid to gas. Even though the second NPT simulation was aborted, it is still useful to analyze the system's behavior a bit more.

In Figure 13, the processed ideal gas quantity or the product of the pressure and volume divided by the temperature is given and plotted as a function of time. When we say "processed", we mean that it has been averaged over every ps in time and filtered twice with a Savitzky-Golay filter to reduce an abundance of noise. In theory, this ideal gas quantity should only be constant for an ideal gas. As the system of TiBr₄ should include intermolecular interactions, this quantity should not be constant. However, from the plot, the possibility of the oscillating behavior after 200 ps being purely because of noise effects cannot be fully ignored. This would suggest ideal gas behavior and that this method of predicting melting points fails to account for Van der Waals interactions. It should be noted that for TiBr₄, only relatively weakly interacting van der Waals interactions have been predicted (Webb & Gordon, 1999). Taking into account the low experimental melting point of 311.4 K \pm 0.1 K and low boiling point of 503 K (Glushko & Gurvich, 1988), and CHGNet previously underestimating the forces, it is reasonable to believe that the Van der Waals interactions are not (sufficiently) present.

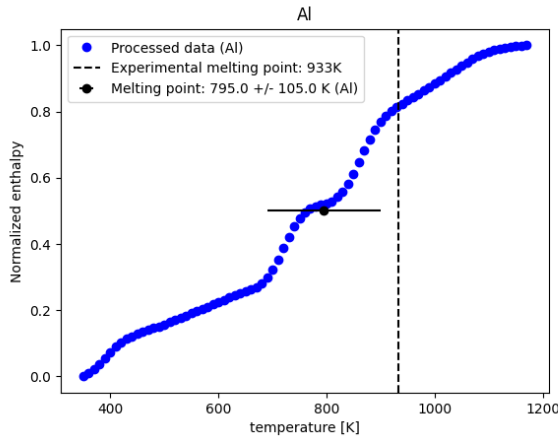


Figure 9: Processed (averaged out every 10K and filter) normalized enthalpy with respect to temperature of the heating curve simulations with CHGNet (ase) of Al for a 7x7x7 supercell.

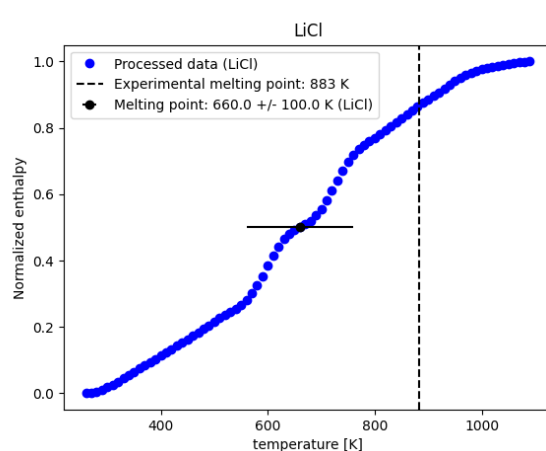


Figure 10: Processed (averaged out every 10K and filter) normalized enthalpy with respect to temperature of the heating curve simulations with CHGNet (ase) of a LiCl supercell containing 432 atoms.

4. TiI₄

For TiI₄, a supercell containing 480 atoms, a starting temperature of 100 K, and an end temperature of 1500 K was used. The result of the second NPT simulation is again visualized on a temperature-time plot in Figure 11 in green. From Figure 12, we obtain results similar to those of TiBr₄, although now the three regimes are somewhat more challenging to distinguish from each other. After investigating the processed ideal gas quantity in Figure 13, similar results appear, suggesting the possible absence of Van der Waals interactions here as well. As the experimental melting point of TiI₄ is 428 K \pm 1 K (Glushko & Gurvich, 1988), this further supports the evidence that the heating curve method, CHGNet, the implementation in ase, or the combination of the three are unable to predict relatively low melting points.

5. WCl₆

For WCl₆, a supercell containing 448 atoms, a starting temperature of 100 K, and an end temperature of 1200 K was used. The result of the second NPT simulation is again visualized on a temperature-time plot in Figure 11 in blue. From Figure 12, we obtain results similar to those of TiBr₄, only now the three regimes are even more challenging to distinguish from each other. After investigating the processed ideal gas quantity in Figure 13, similar results appear, again hinting at the absence of Van der Waals interactions here as well. With the experimental melting point of WCl₆ being 556 K \pm 1 K (Glushko & Gurvich, 1988), this is in accordance with the results from TiBr₄ and TiI₄.

D. Intermediate discussion

The melting points prediction error can be derived from mainly two factors: the force field (i.e. CHGNet), and the simulation. Universal interatomic potentials like CHGNet can not perfectly describe the potential energy surface that's calculated from DFT. The underlying reason mainly comes from the fact that

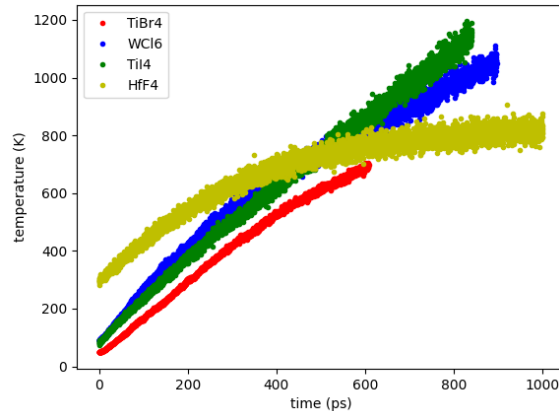


Figure 11: Temperature with respect to time of the heating curve method's second NPT simulation with CHGNet (ase) of HfF₄, TiI₄, TiBr₄ and WCl₆.

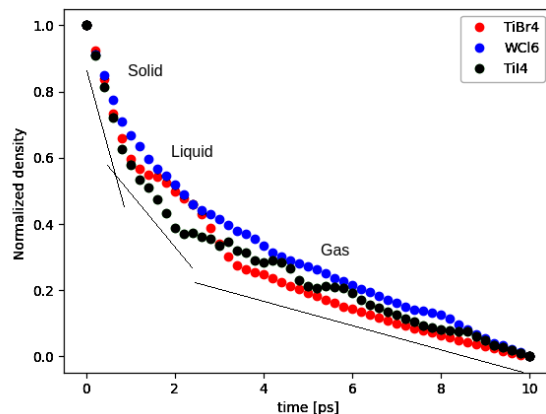


Figure 12: Density with respect to time of the heating curve method's first NPT simulation with CHGNet (ase) of TiBr₄, TiI₄ and WCl₆. The thin black lines indicate the 3 regimes, from left to right, of the solid, liquid and gaseous state.

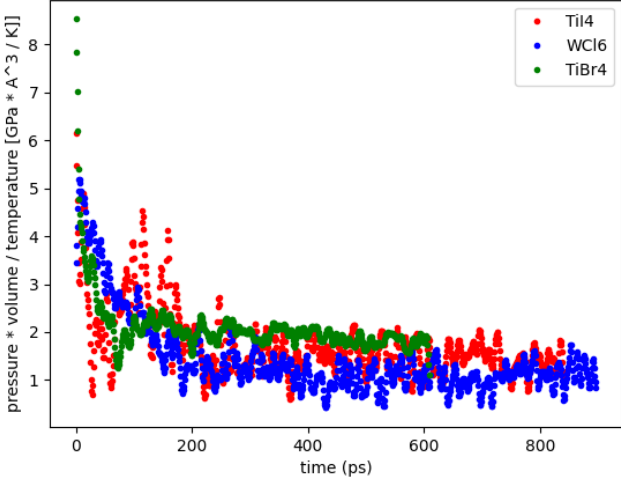


Figure 13: Processed (averaged out every 1 ps and filter) ideal gas quantity with respect to time of the heating curve method’s second NPT simulation with CHGNet (ase) of TiBr_4 , TiI_4 and WCl_6

the training data of MLIPs like CHGNet only represents a limited sub-space of the high-dimentional PES. Specifically, the training data of CHGNet are extracted from DFT ionic relaxations, which mostly characterize near-equilibrium structures. Considering that melting simulations mostly consists of high-energy transition states, it’s hard to generalize to these areas in the PES from purely ionic relaxation data. Another important factor derives from the reliability of training data itself. CHGNet has been trained on mostly GGA and GGA+U DFT labels, and such functionals were found to produce wrong melting points in multiple systems, since interactions like Van Der Waals force are missing.

Apart from the flaws in CHGNet, additional problems may lie within the simulation method. There might have been finite size effects due to the periodic boundary conditions, and the default pressure coupling constant (2 ps) might be too small for these types of simulations. Furthermore, CHGNet is implemented in ASE. ASE uses a Berendsen NPT ensemble algorithm, while LAMMPS relies on the Nosé-Hoover algorithm. Moreover, the ASE documentation even mentions that the available Berendsen method does not result in proper NPT sampling (Larsen et al., 2017b). Additionally, the Nosé-Hoover thermostat produces more realistic fluctuations in the system’s temperature than the Berendsen thermostat. This is because the Nosé-Hoover thermostat does not directly couple the system to a heat bath, as the Berendsen thermostat does. Instead, the Nosé-Hoover thermostat uses a fictitious degree of freedom to control the system’s temperature, allowing the system to fluctuate freely. This characteristic results in more realistic temperature fluctuations in the system. For this reason, the Nosé-Hoover thermostat is better suited for simulations of systems with phase changes (Rühle, 2007). All of the above nuances make it difficult to quantify the CHGNet error in predicting melting points. That’s why a new method is needed.

E. Two phase coexistence method

As the two phase coexistence method does not change the volume of the system, and the systems will not grow unbounded in size, this method is particularly interesting to study, especially considering that TiI_4 , TiBr_4 , and WCl_6 expanded without bounds as a gas using the Heating Curve Method. The two phase coexistence method was applied in the following way: Firstly, a solid is created by constructing a parallelepiped/cuboid supercell with as many copies of the unit cell as possible, while containing fewer than 600 atoms. This supercell has an additional condition that its length should always be five times longer than its width and height. The first condition, regarding the number of atoms, is necessary to limit computational costs. The latter condition is to ensure that the entire supercell is not dominated by interface effects. Avoiding this is essential because, in the end, solid, interface, and liquid regions are required for phase coexistence. Secondly, the liquid is created by heating the solid with an NVT simulation to a temperature well above the experimental melting point retrieved from (Glushko & Gurvich, 1988). Afterward, the structure’s progress through the NVT simulation is monitored in OVITO (Stukowski, 2009) to ensure it has melted. From the solid and liquid, a combined structure is created by merging both along the x-direction, resulting in a new structure, a junction, with twice the original length. As an additional test, the pair correlation of this junction can be plotted. This plot should exhibit distinct peaks from the solid and some form of baseline (which doesn’t have to be constant) from the liquid. Subsequently, a NVE simulation is conducted on the junction. It is important to note that in previous simulations, a timestep of 2 fs was always sufficient. However, for the NVE simulation, a 1 fs timestep was necessary to ensure the conservation of energy. Finally, the NVE simulation is analyzed to determine temperature and pressure convergence.

The two-phase coexistence method encountered several issues rather quickly. The atoms at the interface were merged too closely, resulting in significant forces and excessive energy at the interface. This caused the system to fully melt, and its energy grew unbounded. Furthermore, the pressure was not fixed at 0 GPa. To address these issues, several measures were taken: before the NVE simulation, ionic relaxation was performed without changing the volume to relax the atoms at the interface. Following this, the temperature was initialized by applying a Maxwell-Boltzmann distribution at 1000K to the system. To resolve the pressure problem, in the ideal case, multiple simulations can be performed with different starting volumes, which would affect the final pressure. From these simulations, an extrapolation to the melting point at $P = 1$ atm can be conducted. In light of the unexpected CHGNet Heating Curve predicted melting point of LiCl, it is advisable to include less screened materials like LiF and better screened materials such as Li_2S . It should be noted that because determining the efficiency of CHGNet in pre-

dicting melting points takes priority over calculating halide melting points, this part of the study is no longer limited to halides. Therefore, more similar molecules are tested. Specifically, the following lithium salts: LiCl, Li₂O, Li₂S, Li₂Se, Li₃N, LiBr, LiF, Li₂CO₃. As an example, the full analysis of aluminum and LiCl is presented here. For the other molecules, only the final results are provided. The analyzed figures (displacement and temperature evolution) for these other molecules are available upon request. It is important to note that, similar to the heating curve method, the simple case of aluminum is also tested with the aim of facilitating a more straightforward comparison of the outcomes and cultivating a foundational understanding of the two-phase coexistence method.

1. Al

As with the previous method, before testing more complex structures, it is interesting to examine the simple case of aluminum. For aluminum, only one simulation was required with an initial temperature of 1000K. It should be noted that due to equipartition, after initializing a temperature, T_i , as done through velocity scaling, the temperature drops. This is because the added energy, which initially consists purely of kinetic energy, splits into two components: kinetic energy and potential energy. In other words, kinetic energy transforms into potential energy within the potential well. Please note that this may affect the displacement concerning the first frame. Nevertheless, since this effect is negligible, and the displacement is always recalculated with respect to the 150 ps frame as the reference frame, it is not a concern in this analysis.

The last frame of the system and its color coded displacement, with the initial frame taken as the reference frame, is shown in Figure 14 . From this Figure we clearly observe that the solid-liquid interface remained intact during the NVE simulation. Furthermore, the mean square displacement of the atoms in the solid is limited to approximately 4 Å, while the atoms of the liquid show a mean square displacement range of approximately 4 Å - 10 Å, in which most of the liquid atoms lie. The last frame of the system and its color coded displacement, with the 150 ps frame taken as the reference frame, is shown in Figure 14. Changing the reference frame to the 150 ps frame now gives a picture of the displacement during the last 50 ps of the simulation (instead of the full 200 ps). From these last 50 ps, it is observed that the solid atoms have nearly no to relatively little displacement, which makes sense for a solid. As for the liquid atoms, some of them at the border seem to have solidified, moving the solid-liquid interface by a small amount. Nevertheless, all the other previously liquid atoms have remained liquid, successfully keeping the initial two phase coexistence. Because of this the final temperature of the system can be used as melting point.

In Figure 17 the pressure-time plot of the NVE sim-

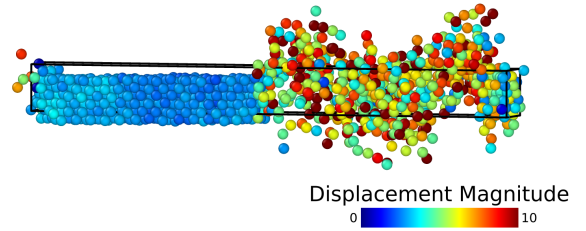


Figure 14: Last frame of the NVE with the Al junction with $T_i = 1000\text{K}$, with the initial frame as the reference frame for the color coded mean square displacement (in Å).

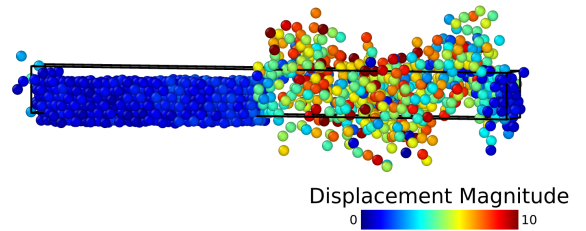


Figure 15: Last frame of the NVE with the Al junction with $T_i = 1000\text{K}$, with the 150 ps frame as the reference frame for the color coded mean square displacement (in Å).

ulation is shown and in Figure 16 the temperature-time plot of the NVE simulation is shown. From both plots we can clearly see that equipartition, as previously mentioned, almost instantly takes effect. For good measure, the final values of the melting point are calculated using only the last 30 % of the date, in this case, the last 20 ps. Nonetheless is it quite difficult to determine convergence from these plots. Because of this a longer simulation time is needed. Therefore the other simulations are done with a simulation time of 200 ps. From both plots we can conclude that the melting point of Al is 805.73 ± 31.94 K at a pressure of 3.82 ± 0.2 GPa. From both experimental and computational work it has been observed that the general trend for the melting point of aluminum is the following: The lower the pressure, the lower the melting point (Hänström & Lazor, 2000; Boehler & Ross, 1997; Vocablo & Alfe, 2002). From the results of Hänström & Lazor, 2000, we even expect the melting point of aluminum with this pressure to be around 1100 K. Therefore the CHGNet two phase coexistence method predicted melting point is completely off. However, it should be noted that the system is possibly not in equilibrium, as it is not easy to determine whether or not the system's quantities converge due to the noise, as can be seen in Figure 16 and Figure 16.

2. LiCl

For LiCl and the other molecules (except for Al) it should be mentioned that the ionic relaxation of the

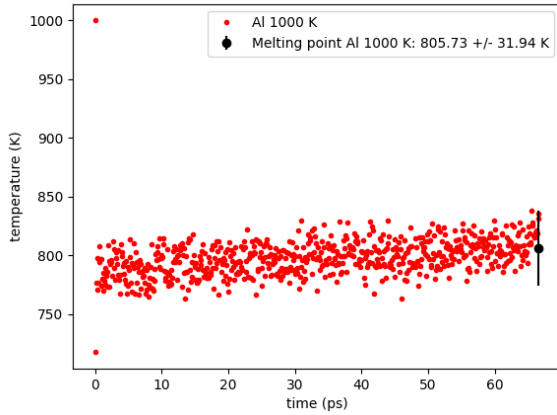


Figure 16: Temperature-time plot of the Al NVE simulation with $T_i = 1000\text{K}$.

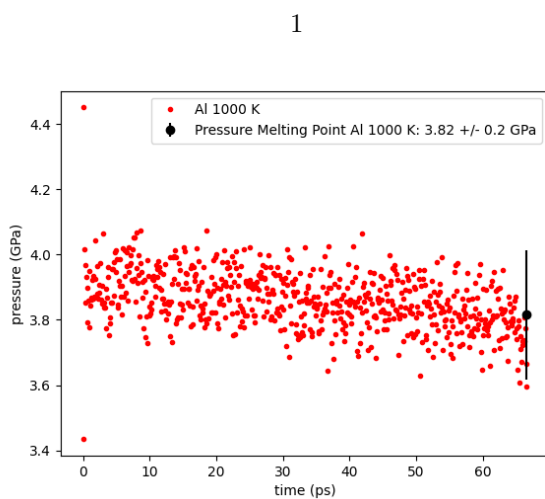


Figure 17: Pressure-time plot of the Al NVE simulation with $T_i = 1000\text{K}$.

junction did not suffice to not have systems with an enormous amount of energy). Therefore in merging the solid and liquid a vacuum with a length of 2\AA was created. Adding this step to the procedure successfully solved the issue for the lithium salts. For LiCl, four different temperatures were initialized: 1600 K, 2000 K, 2300 K and 2600 K. The results of the temperature evolution of the four simulations are shown in Figure 18. Examining this figure, we observe the convergence of the simulations. From this convergence, a melting point is predicted. Care should be taken because not all of the shown melting point predictions are correct. Nevertheless, unlike the simulations using aluminum, there is no question whether or not the system has truly converged. Further analysis is needed to determine the ability of the system to sustain the solid-liquid interface.

Starting with the simulation with $T_i = 2300\text{ K}$ ($T_i = 2600\text{ K}$ has similar results), the system and its color coded displacement are shown in Figure 19 with the 150 ps taken as the reference frame. From this figure, we observe that most of the atoms have a displacement $\geq 4\text{\AA}$. Given the previous aluminum simulation, this marks the system as fully melted. With the solid-liquid interface disappearing, it is not possible to use this simulation to predict a melting point. Second, the simulation with $T_i = 2000\text{K}$, its system and displacement, with the first frame as the reference frame, are shown in Figure 20. From this figure, a distinct fluid and solid structure is observed. To be completely certain, however, it is necessary to look at the displacement results for a different reference frame.

The system and its displacement with the 150 ps frame as the reference frame are shown in Figure 21. The changes in displacement immediately stand out in this figure. However, keep in mind, when interpreting these figures, that the color and thus displacement range can differ. For instance, it makes more sense to put the displacement within the last 50 ps of the simulation on a scale of 0\AA to 10\AA , compared to 0\AA to 20\AA for the displacement during the full 200 ps simulation, as we expect the displacement to be smaller. It is clear that only a small part of the system still contains enough atoms with a displacement larger than 4\AA , during the last 50 ps to indicate the presence of a liquid. As we know from Figure 18 that the system is in equilibrium, this most definitely counts as a valid two phase coexistence simulation and thus a valid melting point prediction. Figure 22 shows the pressure-time plot of the NVE simulation. From Figure 18 and Figure 22, a melting point of $1179.94 \pm 65.89\text{ K}$ and a pressure of $4.34 \pm 0.26\text{ GPa}$ are obtained. For the record, the result for the simulation with $T_i = 1600\text{ K}$ is also shown in Figure 23. Almost all atoms have a displacement smaller than 4\AA . From this we deduce that the structure is almost fully solidified. Therefore, this is not a reliable simulation for use in melting point prediction. Finally, it should be noted that we also observe (from Figure 19, 20 and 21) that the Li-ions (larger circles) are much more mobile than the Cl-ions (smaller circles). This is not surprising as this is also the case

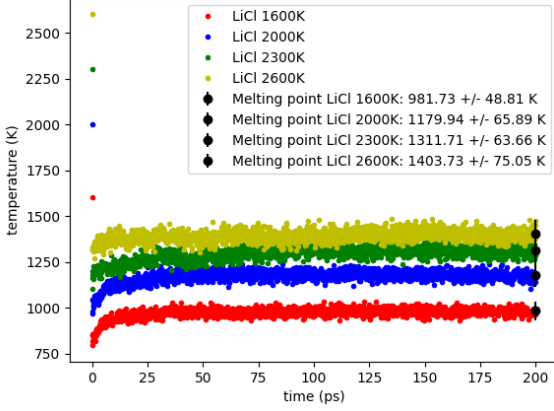


Figure 18: Temperature-time plot of the LiCl CHGNet two phase coexistence NVE simulations. The four initial temperatures are shown, together with the predicted melting points.

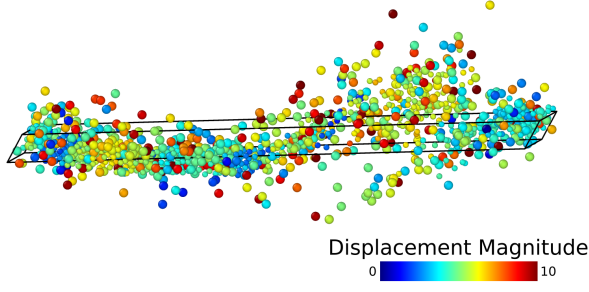


Figure 19: Last frame of the NVE with the LiCl junction with $T_i = 2300\text{K}$, with the 150 ps frame as the reference frame for the color coded mean square displacement (in Å).

for LiCl diluted in water (Koneshan et al., 1998).

3. Li_2O

For Li_2O , there are only ambiguous results. The simulation with $T_i = 2600\text{K}$, the system and displacement, with the 150 ps frame as the reference frame, are shown in Figure 24. Note that this figure differs from the other figures as the trajectories are not unwrapped and atom positions are mapped back into the system cell because of the periodic boundary conditions. Thus, the following is more easily observed: while the lithium atoms with their high mobility are almost entirely in the liquid state, the oxygen atoms are predominantly in the solid state. Therefore, it is not possible to determine the melting point for this structure. The lowest final temperature and pressure for this observed behavior are $1170.69 \pm 51.49 \text{ K}$ and $5.56 \pm 0.35 \text{ GPa}$, respectively.

4. Li_2CO_3

For Li_2CO_3 , a melting point of $553.55 \pm 23.2 \text{ K}$ was predicted at a pressure of $1.39 \pm 0.67 \text{ GPa}$.

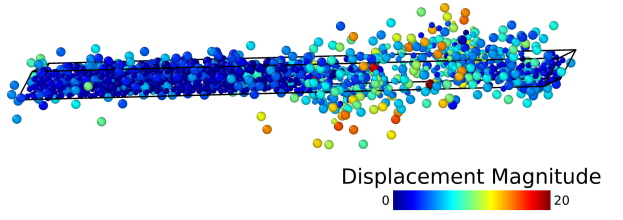


Figure 20: Last frame of the NVE with the LiCl junction with $T_i = 2000\text{K}$, with the initial frame as the reference frame for the color coded mean square displacement (in Å).

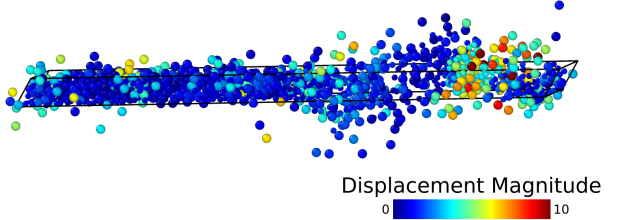


Figure 21: Last frame of the NVE with the LiCl junction with $T_i = 2000\text{K}$, with the 150 ps frame as the reference frame for the color coded mean square displacement (in Å).

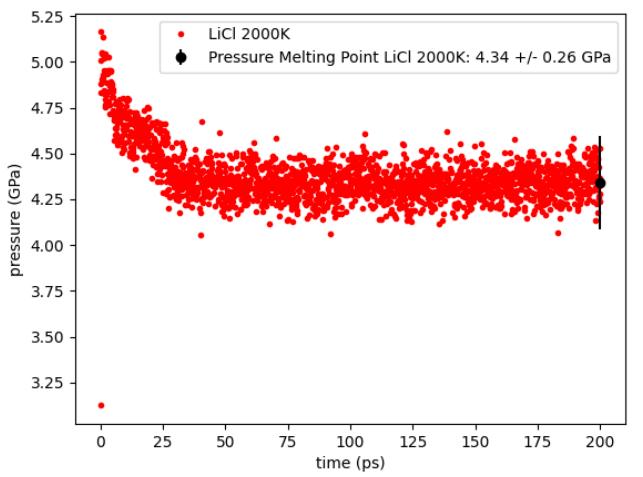


Figure 22: Pressure-time plot of the LiCl NVE simulation with $T_i = 2000\text{K}$.

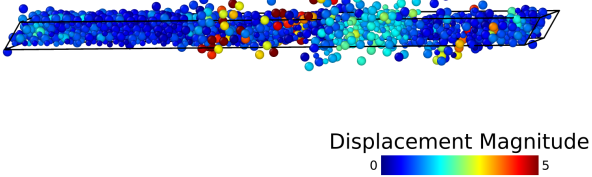


Figure 23: Last frame of the NVE with the LiCl junction with $T_i = 1600\text{K}$, with the 150 ps frame as the reference frame for the color coded mean square displacement (in Å).

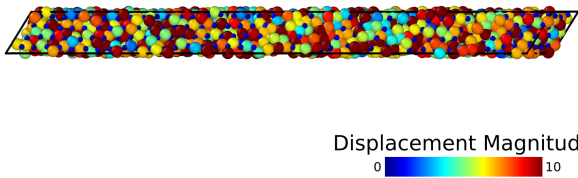


Figure 24: Last frame of the NVE with the Li₂O junction with $T_i = 2600\text{K}$, with the 150 ps frame as reference frame for the color coded mean square displacement (in Å). Note that the trajectories are not unwrapped in this figure.

5. Li₂S

For Li₂S, two melting points were predicted. The results are a melting point of $884.91 \pm 49.5\text{ K}$ at a pressure of $2.94 \pm 0.22\text{ GPa}$ and a melting point of $840.85 \pm 48.33\text{ K}$ at a pressure of $2.66 \pm 48.33\text{ K}$. Both results come from simulations with two phase coexistence present after the NVE simulation. Therefore, further analysis is needed to resolve these ambiguities. Because of this, in Figure 25, the temperature-time plot of both simulations is shown, with a slight modification. The melting temperatures are also plotted as a horizontal line, making it easier to determine whether the system converges or not. From the figure, we observe that only the simulation with the highest predicted melting point truly converges, unlike the other simulation, which has not reached equilibrium within the 200 ps simulation time. Therefore $884.91 \pm 49.5\text{ K}$ at a pressure of $2.94 \pm 0.22\text{ GPa}$ is the true predicted melting point of Li₂S.

6. Li₂Se

For Li₂Se, the predicted melting point is $662.17 \pm 33.5\text{ K}$ at a pressure of $2.53 \pm 0.16\text{ GPa}$.

7. Li₃N

For Li₃N, the predicted melting point is $417.70 \pm 21.46\text{ K}$ at a pressure of $0.15 \pm 0.32\text{ GPa}$.

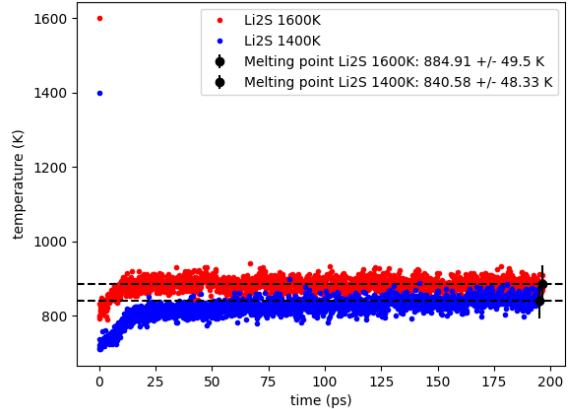


Figure 25: Temperature-time plot of Li₂S CHGNet two phase coexistence NVE simulations. The $T_i = 1600\text{K}$ and $T_i = 1400\text{K}$ simulations are shown together with the predicted melting points.

8. LiBr

For LiBr, similar to Li₂S, there are two predicted melting points. Both simulations again maintain the two phase coexistence. Only now, both converge properly. Therefore, we have a predicted melting point of $497.56 \pm 25.37\text{ K}$ at a pressure of $0.52 \pm 0.11\text{ GPa}$ and a melting point of $473.14 \pm 32.79\text{ K}$ at a pressure of $0.52 \pm 0.14\text{ GPa}$. As both pressures are almost identical and both melting points are within one another's error-range, it can be useful to define a melting point based on the average of both. This results in a melting point of $485.35 \pm 29.08\text{ K}$ at a pressure of $0.52 \pm 0.125\text{ GPa}$.

9. LiF

For LiF, all simulations solidified. The highest observed temperature and pressure were $1541.44 \pm 66.74\text{ K}$ and $9.81 \pm 0.39\text{ GPa}$, respectively.

F. Discussion

An overview of the predicted melting points is given in Table 1. In this table, the predicted melting point temperature, T_{pred} , and pressure, P_{pred} , the experimental melting points at a pressure of 1 atm, $T_{exp,1atm}$, together with an estimate of the experimental melting point at the predicted pressure, $T_{exp,pred,P}$, when available, are shown. Note that given more time, ideally, a larger number of simulations are performed as to interpolate the data to a pressure of 1 atm.

For aluminum, similar to the heating curve simulations, the melting point prediction is below the experimental melting point. The reason why the heating curve method provided a more accurate result (melting point prediction closer to the experimental value) can be explained by the aforementioned superheating effect. As CHGNet underestimates the forces, in both methods, CHGNet predicts a lower melting point. Due to the superheating effect, however, this effect is less noticeable for the heating curve simulations.

For LiCl, the highest observed experimental melting point is 1100 ± 5 K at a pressure of 2.3 GPa (Clark Jr, 1959). By performing quite extreme (doubling the pressure range of the known data points) extrapolations, it is possible to obtain an estimate for the pressure from Clark Jr, 1959 and from Arafin & Singh, 2017. From these (linear) extrapolations, we obtain an estimated melting point of approximately 1543 K and 1768 K, respectively, at 4.34 GPa. If these were to be sufficiently accurate, this would mean that the CHGNet again underestimated the melting point. Although this would fit the established narrative of this study, care should be taken as the linearity assumed in this extrapolation might not be completely accurate.

For Li_2O , the ambiguous results of lithium melting and oxygen solidification are possibly related to the high experimental melting point. For LiF, due to the high pressure (≈ 9 GPa), the results should no longer be compared to the experimental melting point measured at a pressure of 1 atm. From Arafin & Singh, 2017, it is known that the melting temperature at this high pressure is approximately 1700 K. Therefore, the high pressure explains why even the highest temperature simulation (1541.44 ± 66.74 K) solidifies. It should also be noted that LiF is a less screened material in the data used by CHGNet. For this reason, some prediction power might be lost. Li_2S , being a better screened material, also lacks accuracy; therefore, materials being less or more present in the dataset CHGNet is trained on cannot be the only factor.

For Li_2S and all the other materials in Table 1 that weren't mentioned yet, it is quite noticeable that the predicted melting points are roughly only half of the experimental melting points. This could be because of the large observed pressure (1 GPa = 9 869 atm) compared to the 1 atm pressure from which the experimental melting points are observed. However, as we expect the observed melting temperature to be higher than or equal to the experimentally measured melting temperature at a pressure of 1 atm (LiBr in Owens, 1966; lithium salts studied in Pistorius, 1967; alkali halides studied in Arafin & Singh, 2017), this is highly unlikely. Therefore, we can be certain that CHGNet generally underestimates melting points. From this, we can deduce that CHGNet fails to realistically describe fundamental interactions between particles.

Research has shown that long-range van der Waals forces are not accounted for in (meta-)GGA approximations (Langreth et al., 2005; Kothakonda et al., 2022). Knowing that CHGNet uses GGA + U and $r^2\text{SCAN}$ -DFT static calculations (B. Deng et al., 2023), this could explain why CHGNet underestimates the forces between the particles and therefore underestimates the melting points. In these calculations, $r^2\text{SCAN}$ is a revision of the strongly constrained and appropriately normed (SCAN) meta-generalized gradient approximation (meta-GGA), and the +U correction is often interpreted as a simple material-dependent self-interaction correction (Kothakonda et al., 2022; Cococcioni & De Gironcoli, 2005).

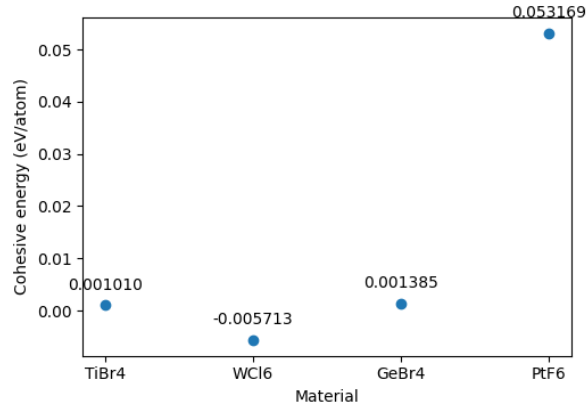


Figure 26: Cohesive energy [eV/atom], calculated using CHGNet, of four 0-dimensional molecules: TiBr_4 , WCl_6 , GeBr_4 and PtF_6

To further validate this hypothesis it is possible to calculate the cohesive energy of a small number of structures using CHGNet. In this context, cohesive energy is the energy needed to transform one mole of a (crystalline) solid at 0 K to isolated (gas-phase) molecules (Kittel, 2005). For simplicity, the cohesive energy of four molecules with a 0-dimensional structure was calculated. The results are shown in Figure 26. It is known that the cohesive energy ranges from 0.1 eV/atom for solids, which can muster only the weak van der Waals bond to 7 eV/atom or more in some covalent and ionic compounds and some metals (Blakemore, 1985). As all of the predicted cohesive energies lie far below 0.1 eV/atom, this confirms our theory. Therefore, we can conclude that CHGNet does not predict the Van Der Waals forces sufficiently accurate to predict melting points.

A possible solution is to include a VV10 dispersion correction or the rVV10 correction in the calculations on which CHGNet is based. The VV10 dispersion correction is fundamentally constructed to yield realistic long-range van der Waals interactions (Vydrov & Van Voorhis, 2010). The rVV10 correction emulates the performance of VV10 but (within a plane-wave-based code) avoids the cost of numerical double integration over 3D space (Sabatini et al., 2013). Although the rVV10 van der Waals correction does not improve upon the volumes predicted by SCAN, $r^2\text{SCAN}+\text{rVV10}$ improves slightly on $r^2\text{SCAN}$ with a 0.5 Å³/atom mean absolute error (Kothakonda et al., 2022). Even though it is only a small improvement, it might have a considerable impact on melting point simulations.

	T_{pred} [K]	P_{pred} [GPa]	$T_{exp,1atm}$ [K]	$T_{exp,pred.P}$ [K]
Al	805.73 ± 31.94	3.82 ± 0.2	933.52 ± 0.1	1100
LiCl	1179.94 ± 65.89	4.34 ± 0.26	883 ± 2	1543 ± 5
Li ₂ O	/	/	1726 ± 5	/
Li ₂ CO ₃	553.55 ± 23.2	1.39 ± 0.67	1038 ± 5	/
Li ₂ S	884.91 ± 49.5	2.94 ± 0.22	1643 ± 10	/
Li ₂ Se	662.17 ± 33.5	2.53 ± 0.16	1576 ± 10	/
Li ₃ N	417.70 ± 21.46	0.15 ± 0.32	1086 ± 2	/
LiBr	485.35 ± 29.08	9.81 ± 0.39	823 ± 2	/
LiF	/	/	1122.05 ± 1	1700

Table 1: Predicted melting point temperature, T_{pred} , and pressure, P_{pred} , experimental melting point at a pressure of 1 atm, $T_{exp,1atm}$, estimate of the experimental melting point at the predicted pressure, $T_{exp,pred.P}$, of the two phase coexistence method using CHGNet.

Conclusion

From the heating curve method and the surrounding literature study, it can be concluded that for future atomistic MD simulations, it might be wise to use a different set of tools such as LAMMPS, unlike ASE that relies on the Berendsen algorithm for the NPT simulations. The heating curve method hinted at the inability of CHGNet to accurately predict melting points through failing simulations (expansion with no limit, similar to an ideal gas) with low experimental melting points. However, for the working melting point predictions of Al and LiCl, the effect of CHGNet underestimating the van der Waals forces was reduced due to the superheating effect. Because of these unwanted effects, a new method was used as to keep the materials from expanding without limit. For this reason the two phase coexistence method was used. From the two phase coexistence melting points were predicted at very high pressures. Although calculated at high pressures, CHGNet often underestimates the melting points by approximately 50%. Subsequently, a short cohesive energy calculation confirmed that CHGNet does not predict the van der Waals forces sufficiently accurate. In conclusion, although CHGNet is a promising model, it strangely fails in determining melting points of halides and other molecules in general.

References

- Abadi, M., Barham, P., Chen, J., Chen, Z., Davis, A., Dean, J., Devin, M., Ghemawat, S., Irving, G., Isard, M., et al. (2016). {Tensorflow}: A system for {large-scale} machine learning. *12th USENIX symposium on operating systems design and implementation (OSDI 16)*, 265–283.
- Abakumov, A. M., Fedotov, S. S., Antipov, E. V., & Tarascon, J.-M. (2020). Solid state chemistry for developing better metal-ion batteries. *Nature Communications*, 11(1), 4976.
- Agrawal, P. M., Rice, B. M., & Thompson, D. L. (2003). Molecular dynamics study of the effects of voids and pressure in defect-nucleated melting simulations. *The Journal of chemical physics*, 118(21), 9680–9688.
- Alavi, S., & Thompson, D. L. (2006). Simulations of melting of polyatomic solids and nanoparticles. *Molecular Simulation*, 32(12-13), 999–1015.
- Arafin, S., & Singh, R. N. (2017). Pressure variation of melting temperatures of alkali halides. *International Journal of Modern Physics B*, 31(5), 1750031.
- Artrith, N., Morawietz, T., & Behler, J. (2011). High-dimensional neural-network potentials for multicomponent systems: Applications to zinc oxide. *Physical Review B*, 83(15), 153101.
- Asano, T., Sakai, A., Ouchi, S., Sakaida, M., Miyazaki, A., & Hasegawa, S. (2018). Solid halide electrolytes with high lithium-ion conductivity for application in 4 v class bulk-type all-solid-state batteries. *Advanced Materials*, 30(44), 1803075.
- Batzner, S., Musaelian, A., Sun, L., Geiger, M., Mailoa, J. P., Kornbluth, M., Molinari, N., Smidt, T. E., & Kozinsky, B. (2022). E (3)-equivariant graph neural networks for data-efficient and accurate interatomic potentials. *Nature communications*, 13(1), 2453.
- Bianchini, M., Lacivita, V., Seo, D.-H., & Kim, H. (2022). Advances and challenges in multiscale characterizations and analyses for battery materials. *Journal of Materials Research*, 37(19), 3113–3129.
- Blakemore, J. S. (1985). *Solid state physics*. Cambridge university press.
- Boehler, R., & Ross, M. (1997). Melting curve of aluminum in a diamond cell to 0.8 mbar: Implications for iron. *Earth and Planetary Science Letters*, 153(3-4), 223–227.
- Chen, C., & Ong, S. P. (2022). A universal graph deep learning interatomic potential for the periodic table. *Nature Computational Science*, 2(11), 718–728.
- Chen, M., Hung, L., Huang, C., Xia, J., & Carter, E. A. (2013). The melting point of lithium: An orbital-free first-principles molecular dynamics study. *Molecular Physics*, 111(22-23), 3448–3456.
- Chokappa, D. K., & Clancy, P. (1987). A computer simulation study of the melting and freezing properties of a system of lennard-jones par-

- ticles: I. melting the solid. *Molecular physics*, 61(3), 597–615.
- Choudhary, K., DeCost, B., Major, L., Butler, K., Thiyyagalingam, J., & Tavazza, F. (2023). Unified graph neural network force-field for the periodic table: Solid state applications. *Digital Discovery*, 2(2), 346–355.
- Clark Jr, S. P. (1959). Effect of pressure on the melting points of eight alkali halides. *The Journal of Chemical Physics*, 31(6), 1526–1531.
- Coccoccioni, M., & De Gironcoli, S. (2005). Linear response approach to the calculation of the effective interaction parameters in the lda+ u method. *Physical Review B*, 71(3), 035105.
- Cole, J. M. (2020). A design-to-device pipeline for data-driven materials discovery. *Accounts of chemical research*, 53(3), 599–610.
- Cygan, R. T., Greathouse, J. A., Heinz, H., & Kalinichev, A. G. (2009). Molecular models and simulations of layered materials. *Journal of Materials Chemistry*, 19(17), 2470–2481.
- Deng, B., Zhong, P., Jun, K., Riebesell, J., Han, K., Bartel, C. J., & Ceder, G. (2023). Chgnet as a pretrained universal neural network potential for charge-informed atomistic modelling. *Nature Machine Intelligence*, 1–11.
- Deng, Z., Kumar, V., Bölle, F. T., Caro, F., Franco, A. A., Castelli, I. E., Canepa, P., & Seh, Z. W. (2022). Towards autonomous high-throughput multiscale modelling of battery interfaces. *Energy & Environmental Science*, 15(2), 579–594.
- Ding, J., Pan, G., Du, L., Lu, J., Wei, X., Li, J., Wang, W., & Yan, J. (2017). Theoretical prediction of the local structures and transport properties of binary alkali chloride salts for concentrating solar power. *Nano Energy*, 39, 380–389.
- Gasteiger, J., Groß, J., & Günemann, S. (2020). Directional message passing for molecular graphs. *arXiv preprint arXiv:2003.03123*.
- Ge, H., Li, H., Mei, S., & Liu, J. (2013). Low melting point liquid metal as a new class of phase change material: An emerging frontier in energy area. *Renewable and Sustainable Energy Reviews*, 21, 331–346.
- Glushko, V. P., & Gurvich, L. (1988). Thermodynamic properties of individual substances: Volume 1, parts 1 and 2.
- Hänström, A., & Lazor, P. (2000). High pressure melting and equation of state of aluminium. *Journal of alloys and compounds*, 305(1-2), 209–215.
- He, K., Zhang, X., Ren, S., & Sun, J. (2016). Deep residual learning for image recognition. *Proceedings of the IEEE conference on computer vision and pattern recognition*, 770–778.
- Hong, Q.-J. (2015). *Methods for melting temperature calculation*. California Institute of Technology.
- Hong, Q.-J., Ushakov, S. V., van de Walle, A., & Navrotsky, A. (2022). Melting temperature prediction using a graph neural network model: From ancient minerals to new materials. *Proceedings of the National Academy of Sciences*, 119(36), e2209630119. <https://doi.org/10.1073/pnas.2209630119>
- Hong, Q.-J., & Van De Walle, A. (2016). A user guide for sluschi: Solid and liquid in ultra small coexistence with hovering interfaces. *Calphad*, 52, 88–97.
- Hu, J., Chen, K., & Li, C. (2018). Nanostructured lithium fluoride coated by ionic liquid as high ion-conductivity solid electrolyte additive to suppress dendrite growth at li metal anode. *ACS applied materials & interfaces*, 10(40), 34322–34331.
- Hutter, J., Iannuzzi, M., Schiffmann, F., & VandeVondele, J. (2014). Cp2k: Atomistic simulations of condensed matter systems. *WIREs Computational Molecular Science*, 4(1), 15–25. <https://doi.org/https://doi.org/10.1002/wcms.1159>
- Jain, A., & Yalkowsky, S. H. (2006). Estimation of melting points of organic compounds-ii. *Journal of Pharmaceutical Sciences*, 95(12), 2562–2618. <https://doi.org/https://doi.org/10.1002/jps.20634>
- Jain, A., Ong, S. P., Hautier, G., Chen, W., Richards, W. D., Dacek, S., Cholia, S., Gunter, D., Skinner, D., Ceder, G., et al. (2013). Commentary: The materials project: A materials genome approach to accelerating materials innovation. *APL materials*, 1(1).
- Jinnouchi, R., Miwa, K., Karsai, F., Kresse, G., & Asahi, R. (2020). On-the-fly active learning of interatomic potentials for large-scale atomistic simulations [PMID: 32787192]. *The Journal of Physical Chemistry Letters*, 11(17), 6946–6955. <https://doi.org/10.1021/acs.jpclett.0c01061>
- Jorgensen, W. L., & Tirado-Rives, J. (1988). The opls [optimized potentials for liquid simulations] potential functions for proteins, energy minimizations for crystals of cyclic peptides and crambin. *Journal of the American Chemical Society*, 110(6), 1657–1666.
- Kästner, J. (2011). Umbrella sampling. *Wiley Interdisciplinary Reviews: Computational Molecular Science*, 1(6), 932–942.
- Kato, Y., Hori, S., Saito, T., Suzuki, K., Hirayama, M., Mitsui, A., Yonemura, M., Iba, H., & Kanno, R. (2016). High-power all-solid-state batteries using sulfide superionic conductors. *Nature Energy*, 1(4), 1–7.
- Khare, S., Dell'Amico, M., Knight, C., & McGarry, S. (2012). Selection of materials for high temperature latent heat energy storage. *Solar energy materials and solar cells*, 107, 20–27.
- Kittel, C. (2005). *Introduction to solid state physics*. John Wiley & sons, inc.
- Ko, T. W., Finkler, J. A., Goedecker, S., & Behler, J. (2021). A fourth-generation high-dimensional neural network potential with accurate electrostatics including non-local charge transfer. *Nature communications*, 12(1), 398.
- Koneshan, S., Rasaiah, J. C., Lynden-Bell, R., & Lee, S. (1998). Solvent structure, dynamics, and ion mobility in aqueous solutions at 25 °C.

- The Journal of Physical Chemistry B*, 102(21), 4193–4204.
- Kothakonda, M., Kaplan, A. D., Isaacs, E. B., Bartel, C. J., Furness, J. W., Ning, J., Wolverton, C., Perdew, J. P., & Sun, J. (2022). Testing the r2scan density functional for the thermodynamic stability of solids with and without a van der waals correction. *ACS Materials Au*, 3(2), 102–111.
- Kwak, H., Wang, S., Park, J., Liu, Y., Kim, K. T., Choi, Y., Mo, Y., & Jung, Y. S. (2022). Emerging halide superionic conductors for all-solid-state batteries: Design, synthesis, and practical applications. *ACS Energy Letters*, 7(5), 1776–1805. <https://doi.org/10.1021/acsenergylett.2c00438>
- Langreth, D. C., Dion, M., Rydberg, H., Schröder, E., Hyldgaard, P., & Lundqvist, B. I. (2005). Van der waals density functional theory with applications. *International journal of quantum chemistry*, 101(5), 599–610.
- Larsen, A. H., Mortensen, J. J., Blomqvist, J., Castelli, I. E., Christensen, R., Dułak, M., Friis, J., Groves, M. N., Hammer, B., Hargus, C., et al. (2017a). The atomic simulation environment—a python library for working with atoms. *Journal of Physics: Condensed Matter*, 29(27), 273002.
- Larsen, A. H., Mortensen, J. J., Blomqvist, J., Castelli, I. E., Christensen, R., Dułak, M., Friis, J., Groves, M. N., Hammer, B., Hargus, C., et al. (2017b). The atomic simulation environment—a python library for working with atoms. <https://wiki.fysik.dtu.dk/ase/ase/md.html#module-ase.md.nptberendsen>
- Larsson Sihm, A. (2019). Melting points of binary and ternary eutectic chloride salts: Md simulations on licl-nacl-kcl and its binary constituents.
- Li, X., Liang, J., Luo, J., Banis, M. N., Wang, C., Li, W., Deng, S., Yu, C., Zhao, F., Hu, Y., et al. (2019). Air-stable li 3 incl 6 electrolyte with high voltage compatibility for all-solid-state batteries. *Energy & Environmental Science*, 12(9), 2665–2671.
- Li, X., Liang, J., Yang, X., Adair, K. R., Wang, C., Zhao, F., & Sun, X. (2020). Progress and perspectives on halide lithium conductors for all-solid-state lithium batteries. *Energy & Environmental Science*, 13(5), 1429–1461.
- Ljungberg, L. Y. (2007). Materials selection and design for development of sustainable products. *Materials & Design*, 28(2), 466–479.
- López-Zorrilla, J., Aretxabaleta, X. M., Yeu, I. W., Etxebarria, I., Manzano, H., & Artrith, N. (2023). ænet-pytorch: A gpu-supported implementation for machine learning atomic potentials training. *The Journal of Chemical Physics*, 158(16).
- Luo, S.-N., Ahrens, T. J., Çağın, T., Strachan, A., Goddard III, W. A., & Swift, D. C. (2003). Maximum superheating and undercooling: Systematics, molecular dynamics simulations, and dynamic experiments. *Physical Review B*, 68(13), 134206.
- Mei, J., & Davenport, J. (1992). Free-energy calculations and the melting point of al. *Physical Review B*, 46(1), 21.
- Mendelev, M., Kramer, M., Becker, C. A., & Asta, M. (2008). Analysis of semi-empirical interatomic potentials appropriate for simulation of crystalline and liquid al and cu. *Philosophical Magazine*, 88(12), 1723–1750.
- Mitchell, M. J., & McCammon, J. A. (1991). Free energy difference calculations by thermodynamic integration: Difficulties in obtaining a precise value. *Journal of computational chemistry*, 12(2), 271–275.
- Morris, J. R., Wang, C., Ho, K., & Chan, C. T. (1994). Melting line of aluminum from simulations of coexisting phases. *Physical Review B*, 49(5), 3109.
- Mroż, A. M., Posligua, V., Tarzia, A., Wolpert, E. H., & Jelfs, K. E. (2022). Into the unknown: How computation can help explore uncharted material space [PMID: 36206484]. *Journal of the American Chemical Society*, 144(41), 18730–18743. <https://doi.org/10.1021/jacs.2c06833>
- Owens, B. (1966). Corresponding-states melting curve for the alkali halides at high pressure. *The Journal of Chemical Physics*, 44(8), 3144–3145.
- Perez, A., Morrone, J. A., Simmerling, C., & Dill, K. A. (2016). Advances in free-energy-based simulations of protein folding and ligand binding [Folding and binding • Nucleic acids-protein complexes]. *Current Opinion in Structural Biology*, 36, 25–31. <https://doi.org/https://doi.org/10.1016/j.sbi.2015.12.002>
- Phillpot, S., Lutsko, J., Wolf, D., & Yip, S. (1989). Molecular-dynamics study of lattice-defect-nucleated melting in silicon. *Physical Review B*, 40(5), 2831.
- Pistorius, C. W. (1967). Phase diagrams of lithium sulphate, selenate and chromate to 40 kbar. *Journal of Physics and Chemistry of Solids*, 28(9), 1811–1819.
- Plimpton, S. (1995). Fast parallel algorithms for short-range molecular dynamics. *Journal of computational physics*, 117(1), 1–19.
- Riebesell, J., Goodall, R. E. A., Jain, A., Benner, P., Persson, K. A., & Lee, A. A. (2023). Matbench discovery – an evaluation framework for machine learning crystal stability prediction.
- Rühle, V. (2007). Berendsen and nose-hoover thermostats. *Am. J. Phys.*, 575.
- Sabatini, R., Gorni, T., & De Gironcoli, S. (2013). Non-local van der waals density functional made simple and efficient. *Physical Review B*, 87(4), 041108.
- Scarselli, F., Gori, M., Tsai, A. C., Hagenbuchner, M., & Monfardini, G. (2008). The graph neural network model. *IEEE transactions on neural networks*, 20(1), 61–80.

- Schafer, R. W. (2011). What is a savitzky-golay filter? [lecture notes]. *IEEE Signal processing magazine*, 28(4), 111–117.
- Simón, L., & Goodman, J. M. (2011). How reliable are dft transition structures? comparison of gga, hybrid-meta-gga and meta-gga functionals. *Organic & biomolecular chemistry*, 9(3), 689–700.
- Singh, J. K., & Kofke, D. A. (2004). Mayer sampling: Calculation of cluster integrals using free-energy perturbation methods. *Physical review letters*, 92(22), 220601.
- Solca, J., Dyson, A. J., Steinebrunner, G., Kirchner, B., & Huber, H. (1997). Melting curve for argon calculated from pure theory. *Chemical physics*, 224(2-3), 253–261.
- Stukowski, A. (2009). Visualization and analysis of atomistic simulation data with ovo—the open visualization tool. *Modelling and simulation in materials science and engineering*, 18(1), 015012.
- Takamoto, S., Izumi, S., & Li, J. (2022). Teanet: Universal neural network interatomic potential inspired by iterative electronic relaxations. *Computational Materials Science*, 207, 111280.
- Takamoto, S., Shinagawa, C., Motoki, D., Nakago, K., Li, W., Kurata, I., Watanabe, T., Yayama, Y., Iriguchi, H., Asano, Y., et al. (2022). Towards universal neural network potential for material discovery applicable to arbitrary combination of 45 elements. *Nature Communications*, 13(1), 2991.
- Thompson, A. P., Aktulga, H. M., Berger, R., Bolintineanu, D. S., Brown, W. M., Crozier, P. S., in't Veld, P. J., Kohlmeyer, A., Moore, S. G., Nguyen, T. D., et al. (2022). Lammps-a flexible simulation tool for particle-based materials modeling at the atomic, meso, and continuum scales. *Computer Physics Communications*, 271, 108171.
- Tkv database. (n.d.). Retrieved September 4, 2023, from <http://www.chem.msu.su/cgi-bin/tkv.pl?show=welcome.html/welcome.html>
- Unke, O. T., Chmiela, S., Gastegger, M., Schütt, K. T., Sauceda, H. E., & Müller, K.-R. (2021). Spookynet: Learning force fields with electronic degrees of freedom and nonlocal effects. *Nature communications*, 12(1), 7273.
- Victor Chombo, P., Laounual, Y., & Wongwises, S. (2021). Lessons from the electric vehicle crash-worthiness leading to battery fire. *Energies*, 14(16), 4802. <https://doi.org/10.3390/en14164802>
- Vocadlo, L., & Alfe, D. (2002). Ab initio melting curve of the fcc phase of aluminum. *Phys Rev B*, 65(21).
- Vydrov, O. A., & Van Voorhis, T. (2010). Nonlocal van der waals density functional: The simpler the better. *The Journal of chemical physics*, 133(24).
- Webb, S. P., & Gordon, M. S. (1999). Intermolecular self-interactions of the titanium tetrahalides tix4 (x= f, cl, br). *Journal of the American Chemical Society*, 121(11), 2552–2560.
- Yang, K., Chen, L., Ma, J., He, Y.-B., & Kang, F. (2021). Progress and perspective of li1+xalxti2-x(po4)3 ceramic electrolyte in lithium batteries. *InfoMat*, 3(11), 1195–1217.
- Zhang, L., Wang, H., Car, R., & Weinan, E. (2021). Phase diagram of a deep potential water model. *Physical review letters*, 126(23), 236001.
- Zhang, Y., & Maginn, E. J. (2012). A comparison of methods for melting point calculation using molecular dynamics simulations. *The Journal of chemical physics*, 136(14).
- Zheng, L., Luo, S.-N., & Thompson, D. L. (2006). Molecular dynamics simulations of melting and the glass transition of nitromethane. *The Journal of chemical physics*, 124(15).
- Zubatyuk, R., Smith, J. S., Nebgen, B. T., Tretiak, S., & Isayev, O. (2021). Teaching a neural network to attach and detach electrons from molecules. *Nature communications*, 12(1), 4870.